Title
Internal mixing dynamics of Cu/Sn-Pb plasmas produced by femtosecond laser ablation

Authors
Hai, Ran
Mao, Xianglei
Chan, George C-Y
et al.

Publication Date
2018-10-01

DOI
10.1016/j.sab.2018.06.009

Peer reviewed

Internal mixing dynamics of Cu/Sn-Pb plasmas produced by femtosecond laser ablation

Ran Hai[a,b], Xianglei Mao[b], George C.-Y. Chan[b], Richard E. Russo[b], Hongbin Ding[a], Vassilia Zorba[b,*]

[a] School of Physics, Dalian University of Technology, Dalian, 116024, PR China
[b] Lawrence Berkeley National Laboratory, Berkeley, CA 94720, USA
* Corresponding author: vzorba@lbl.gov

Abstract

Chemical imaging applications using Laser Induced Breakdown Spectroscopy (LIBS) involve laser ablation sampling at interfaces or boundaries between materials with different thermophysical and optical properties, leading to the formation of two initially isolated plasmas. The mechanisms of mixing in these plasmas and their direct implications on spectral emission and chemical imaging remain largely unknown. We investigate the mixing dynamics of isolated plasmas produced using femtosecond (fs) laser pulses at the interface between two different model Cu and Sn-Pb samples. Specifically, we study the spatial and temporal mixing dynamics and outer plasma expansion dynamics of the fs plasma components. The time-resolved degree of component mixing, horizontal and vertical expansion, mixing speed, and temperature and electron density of the heterogeneous plasma are characterized. Mixing processes are initiated early on, less that 100 nanoseconds after the laser pulse, and continue taking place until the end of plasma emission persistence at a constant velocity of 10^4 cm/s. These findings demonstrate that proper selection of detection timing parameters and signal collection position are critically important in precise LIBS measurements to ensure that full plasma mixing has taken place and that homogeneous spectral emission is properly detected.

Introduction

Laser ablation (LA) is a very active field of research supported by widespread applications ranging from laser-induced breakdown spectroscopy (LIBS) [1], LA inductively coupled plasma optical emission spectrometry (LA-ICP-OES) [2], LA-inductively coupled plasma mass spectrometry (LA-ICP-MS) [3], to pulsed laser deposition (PLD) [4], laser-assisted material synthesis [5] and micromachining [6]. For analytical purposes, laser ablation has been recognized as a powerful tool for direct, real-time analysis of materials without sample preparation. During the past few years, LIBS, an optical emission technique, has emerged as a powerful real-time, chemical analysis tool [8-10]. The technique is based on the detection of spectral emission originating from a plasma formed following the interaction of a pulsed laser beam with a sample. LIBS enables three-dimensional chemical imaging and analysis of samples at atmospheric pressure and without sample preparation [11-13].

Laser pulse duration is an important parameter in establishing the LIBS plasma properties. Unlike nanosecond-pulsed laser ablation with significant thermal behavior, femtosecond ablation is associated with non-linear absorption and non-thermal mechanisms leading to spatially confined laser-material analysis with suppressed thermal effects [14-15]. These characteristics are ideally suited for high spatial (lateral) and axial (depth) resolution imaging and analysis [16, 17].

One of the open questions in LIBS mapping and chemical imaging applications is the role of the sample chemical inhomogeneity on the analytical behavior. Specifically, the laser ablation crater size with respect to the surface roughness and chemical homogeneity of the sample is a very important parameter. For example, when the length scale (beam size) of laser sampling is commensurate to that of the sample chemical heterogeneity, the laser-material interaction, plasma expansion and subsequent spectral emission detection is likely to be influenced at the interface between media with different optical, thermal and physical properties.

There is little known about the spatial and temporal mixing between emitting species within different parts of a laser-induced plasma. Understanding the mixing behavior can be critical to optimizing LIBS signal acquisition with a proper time window, and suitable collection position. Sufficient intermixing between multiple elements to produce a homogeneous plasma has significant advantages for applications in laser ablation chemical analysis as well as in laser ion sources and pulsed laser deposition using multicomponent targets.

In this work we studied spatio-temporal plasma separation and mixing processes at the interface between two model materials, using femtosecond laser ablation. How these processes affect femtosecond LIBS emission is also investigated. Direct plasma imaging of elements of interest and fs-LIBS analysis are used to study the plasma expansion front, expansion and mixing velocities, excitation temperature and electron density of each component in the laser induced plasma. These findings demonstrate the importance of carefully selecting laser sampling and detection parameters in chemical imaging applications with LIBS.

Experimental

A schematic view of the experimental setup for time-resolved imaging of the laser-induced plasma is shown in **Figure 1**. A Ti:Sapphire (800 nm) femtosecond laser (Astrella, Coherent) was used as the ablation source, delivering 46 fs, 3.5 mJ pulses at a repetition rate of 1 Hz. The laser beam was directed normal to the sample surface by 45^{o} mirrors and focused by a plano-convex lens (f=150 mm). In order to avoid air breakdown by the laser pulses, the laser focus position was set 3.5 mm below the sample surface. In this configuration, the diameter of the crater was about 0.2 mm and the irradiance was approximately 2.4×10^{14} W/cm^2.

A Cu/Sn-Pb/Cu three-layer sample was constructed for this work. Two polished pure copper plates (99.95% Cu, Goodfellow) were welded with a Sn-Pb alloy (60% Sn and 40% Pb, Kester) intermediate layer. The thickness of each layer was 3 mm. The three-layer sample was subsequently mechanically polished with silicon carbide (SiC) papers of different grades to ensure a flat surface and then ultrasonically cleaned using ethanol. The resulting average surface roughness Ra was determined as 0.02 μm by using white light interferometry. A Cu region, a Sn-Pb region, and a Cu/Sn-Pb interface region were selected for the ablation studies. Specifically, in the case of the Cu/Sn-Pb interface, the center of laser beam was placed at the interface between Cu and Sn-Pb (inset of **Figure 1**). The sample was mounted on a high precision X-Y-Z translation stage to provide a fresh sample surface for each test, and the sampling position and laser ablation process were monitored via a CMOS camera.

The time resolved expansion of the laser-induced plasma was investigated by using a Czerny-Turner spectrograph (1250 M Series II, Horiba Jobin Yvon) with a 1250 mm focal length coupled with an intensified CCD (ICCD) camera (PI MAX 1300, Princeton Instruments), A grating of 1200 grooves/mm was used for this work. The ICCD was directly triggered by the fs laser and the relative delay was

controlled by the camera. An objective lens (LMU-3X-UVB, Thorlabs) was used to image the plasma onto the entrance slit of the spectrograph / ICCD camera system. The optical axis of the spectrometer was oriented along the x-direction parallel to the sample surface, and aligned parallel to the Cu/Sn-Pb interface (cf. **Figure 1**).

For imaging of the fs laser-induced plasma, the spectrometer was set to zero-order and its entrance slit was widened to 3 mm to record the entire plasma emission. A narrowband FB380-10 filter (center wavelength 380 nm, FWHM 10 nm) and an FL514.5-10 filter (center wavelength 514.5 nm, FWHM 10 nm) were sequentially placed in the detection optical path to collect the Sn and Cu atomic emission, respectively. By using a calibrated fine-resolution test target (1951 USAF Target, Thorlabs), the magnification and pixel calibration of the combined ICCD spectrometer and imaging lens system were directly measured as 6× and 3.3 μm/pixel, respectively. The system provided enough depth of field to clearly resolve the expanding plasma.

For wavelength-resolved plasma imaging studies, the entrance slit of the spectrometer was set at 120 μm to collect enough photons while providing sufficiently good spectral resolution for LIBS analysis. Because the magnification of the system was 6×, the spectrometer-detector system measured a 20 μm-wide slice of the plasma, located along the Z direction (vertical plasma expansion direction - **Figure 1**). In order to record the emission from different sample positions along the Y direction, the imaging objective lens was translated along the Y axis. Following ablation, the crater profiles were measured using white-light interferometry (New View 6K, Zygo Corporation). The ablation depths per pulse of Cu and Sn-Pb were approximately 0.2 and 1.4 μm/pulse, respectively.

Results and Discussion

Femtosecond laser-induced plasma imaging

ICCD imaging provides two-dimensional snapshots of the expanding laser-induced plasma. **Figure 2** shows time-resolved images of pure Cu, Sn-Pb and Cu/Sn-Pb plasmas acquired under the same experimental conditions. Representative images were captured after the laser pulse (t=0) at different gate integration widths. After conditioning the surface with 5 laser pulses, 20 individual ICCD images were recorded at the same delay time, at every distinct sampling location. For clarity, each image is normalized to its maximum intensity.

Figures 2a and **2c** show the images of Cu atomic emission at the Cu/Sn-Pb interface and from pure Cu ablation, respectively. The images were captured using a dielectric narrow bandpass filter centered at 514.5 nm (FWHM 10 nm), which overlaps with the Cu atomic lines at 510.55 nm, 515.32 nm and 521.82 nm. At the early stages of plasma formation (0-25 ns), the measured emission at the Cu/Sn-Pb interface (**Figure 2a**) is similar to that of the pure Cu plasma (**Figure 2c**), because the Cu and Sn plasmas emit predominantly a continuum spectrum (such as Bremsstrahlung and recombination radiation).

As the plasma cools, the continuum background decayed significantly, making it possible for the Cu atomic emission to be observed. The ratios of Cu atomic emission intensity to the continuum background at 0-25 ns and 50-100 ns were 0 and 10%, respectively. After 50 ns, a clearer boundary between the Cu and Sn-Pb plasmas was observed in the direction normal to the sample surface. This boundary slowly moves towards the opposite sample side with time (i.e. Cu emission in the Sn-Pb sample side, and vice versa). After 400 ns, part of the Cu plasma partially moved in the direction of the Sn-Pb interface and within 1.6 μs it had transitioned well into the Sn-Pb plasma region.

Time resolved images of Sn atomic emission generated at the Cu/Sn-Pb interface and at the pure Sn-Pb alloy area, are shown in **Figures 2b** and **2d**. The laser-induced plasma emission was filtered spectrally by a narrow bandpass filter (FWHM 10 nm) which was centered near the Sn atomic line at 380.10 nm. At early delay times ($t<50$ ns), strong continuum emission over the same bandpass range masked the Sn atomic emission from the Sn-Pb sample. Mixing of Sn and Cu plasmas was observed over a range of temporal delays from 100 to 800 ns.

In order to investigate the mixing behavior within the plasma at early times, the continuum emission was subtracted from the total emission signal. Time- and space-resolved spectra were acquired to obtain the ratios of the peak intensity of emission lines over the total emission intensity in order to correct the ICCD images. Five distances across the Cu/Sn-Pb plasma along the *Y* horizontal direction (*Y*=-150, -75, 0, 75 and 150 μm) were selected. The position of the detection system objective lens was adjusted for every location to ensure that the entire spectral emission was captured accurately.

In **Figure 3**, *Y*=0 μm represents the interface between the Cu and Sn-Pb alloys. Negative values correspond to the Cu side, whereas positive values correspond to the Sn-Pb side. Positions *Y*=-75 μm and *Y*=75 μm correspond to the centers of the Cu and Sn-Pb alloy plasmas, respectively, and *Y*=-150 μm and *Y*=150 μm represent the outer edges (see **Figure 1** inset). **Figures 3a** and **3b** show plots of the fs laser induced plasma spectra obtained through two separately used narrowband filters (centered around 380 nm and 514.5 nm), at the five representative locations between the two edges at a delay time of 100 ns. Spectra

collection with the same filters corresponding to plasma imaging ensured the calculation of the percentage of atomic emission intensity was precise. The spectra were spatially integrated in the Z- direction in order to increase the signal-to-noise ratio. The integrated intensities of the atomic emission lines were obtained by Lorentz profile fitting. The ratios of atomic line emission to the total emission intensity at five positions along Y axis are shown in **Figure 3c**. **Figure 3d** shows the measured depth profile of the Cu/Sn-Pb crater obtained after 5 pulses with the beam center focused at the interface between the two materials. The ablation depths in Cu and Sn-Pb were approximately 1 and 7 μm, respectively, which were significantly smaller than the crater diameter of 200 μm. A low aspect ratio (depth/diameter) crater was chosen to ensure that plasma trapping in high-aspect ratio craters would not take place, and thereby impact the imaging and spectral emission detection [18].

The atomic emission ratio matrix was calculated by analyzing spatially-resolved emission data at different times. A computer program was developed to process the spatio-temporal distributions of Cu and Sn atomic emission from the raw ICCD image data and calculate the space-resolved atomic emission ratio matrices. The calibrated spatial distributions of the time-integrated atomic emission from the Cu and Sn plasmas are shown in **Figure 4**. In order to compare images at different delay times on a same scale, each image has been normalized to its own maximum intensity.

Atomic and ionic line emission at early times (delay ≤ 50 ns) could not be readily identified and isolated from the strong plasma continuum. The atomic line emission became distinct after approximately 50 ns. However, mixing between the Cu and Sn-Pb alloy expanding plasmas is already observable at this early time, likely from the initial lateral (horizontal) expansion of the laser ablated plasma, causing atoms with sufficient horizontal kinetic energy to travel into the other hot and dense plasma region at early times. At later times, the degree of mixing is significantly enhanced.

In **Figure 4,** Z_{Cu} and Y_{Cu} represent the outward vertical and outward horizontal expansion of the plasma, respectively, and M_{Cu} represents the interfacial mixing of Cu into the Sn-Pb plasma. Similarly, Z_{Sn}, Y_{Sn} and M_{Sn} represent the front positions of the Sn plasma expanding vertically, horizontally towards air and mixing into the Cu plasma, respectively.

In order to understand the plasma expansion dynamics and quantify the mixing behavior between Cu and Sn expanding plasmas, we plotted the edge position vs. time (*R-t*) graphs of pure Cu, Sn-Pb and mixed Cu/Sn-Pb plasmas. The plasma edge is defined as the position where the intensity falls to 50% of the maximum.

Figure 5a shows the temporal variation of the outward horizontal (Y_{Cu}, Y_{Sn}) and the vertical plasma expansion fronts (Z_{Cu}, Z_{Sn}) from the pure Cu and Sn-Pb samples, respectively. Following an initial fast expansion, the plasma slowed progressively in both directions due to resistance from collisions with the surrounding gas (ambient air). The outward plasma expansion behavior is in good agreement with the drag model, which is given by [20, 21]

$$R(t)=R_S[1-\exp(-\beta t)]$$

where R_s is the stopping distance of the plasma, and β represents the slowing coefficient ($R_s = v_0/\beta$, v_0 being the initial velocity).

A comparison of the time-resolved horizontal mixing behavior of the Cu and Sn plasmas (M_{Cu}, M_{Sn}) is shown in **Figure 5b**. After 50 ns, the plasma horizontal mixing position for both plasmas followed a linear behavior as a function of time, indicating a relatively free expansion of one plasma component into the other [22]. **Figure 5c** shows the time-resolved horizontal outward expansion velocity of pure Cu and Sn plasma (solid lines), and the horizontal mixing velocities of Cu and Sn-Pb in Cu/Sn-Pb plasmas (dashed lines), calculated from the slopes of the *R-t* plots. The horizontal expansion velocity of the plasma front was maximum at early times before gradually decreasing with time. At 12.5 ns, the calculated outward horizontal expansion velocities of pure Cu and Sn-Pb plasmas were 2.9×10^4 cm/s and 2.5×10^4 cm/s, respectively. The horizontal mixing velocities for Cu and Sn-Pb plasmas were nearly invariant as a function of time (dashed lines in **Figure 5c**) at around 1.2×10^4 cm/s. The outward horizontal expansion velocity of the plasma was significantly higher than the internal mixing velocity at early times (< 200 ns). However, at later times (> 300 ns), the mixing process between the Cu and Sn-Pb plasma components was significantly faster than the outward horizontal plasma expansion.

To quantify the percentage of mixing, we introduced the mixing degree (r) of the plasma emission as the percentage of I_M, which representing the atoms having crossed the vertical plane/interface (Y=0), over the total atomic emission I_T. The value of r lies between 0% and 50%; for an r-value of 0%, no emitting species have crossed the interface to infiltrate the opposite plasma and an r-value close to 50% corresponds to complete homogeneous mixing between the two plasmas. The degree of mixing as a function of time is shown in **Figure 5d**. Approximately 19% of emitting Cu atoms crossed into the Sn-Pb plasma region at 75 ns, when only very weak atomic line emission is observed. Similarly, about 14% of the emitting Sn atoms transitioned into the Cu plasma area at the same time, indicating that the mixing process between the two plasmas was initiated at a time scale of tens of nanoseconds. However, sufficient mixing between the two components (mixing ratio of approximately 50%) was not observed until 1200 ns, which

corresponds to the overall persistence time of plasma emission. At 1200 ns, Cu and Sn plasmas mixed adequately, corresponding to a nearly homogeneous distribution of two species in the plasma.

Plasma properties: electron density (n_e) and excitation temperature (T_{exc})

The electron density (n_e) and the excitation temperature (T_{exc}) are important physical parameters, which can be used in understanding the mixing behavior between emitting species. The electron density can be determined from the spectral line widths, and is affected by the broadening mechanisms originating from the surrounding plasma environment. These atoms and ions are placed under the influence of electric and magnetic fields by moving electrons and ions in addition to electron-atom, ion-atom and atom-atom collisions. Under the present experimental conditions, the contribution from Doppler broadening due to thermal motion of the emitting species was estimated to be in the order of 0.001 nm, which is much less than the observed Stark broadening (**Figure 3**), and therefore, can be neglected. Spectral line broadening in the laser-induced plasma is dominated by Stark broadening due to the electric fields produced by charged particles [23]. The Stark-broadened line was extracted from the measured line width by simply subtracting the instrumental broadening. The instrumental broadening width was 0.102 nm measured from emission lines of a mercury light source. For typical fs-LIBS conditions, the contribution from ion impact broadening is negligible. To a very good approximation, the full width at half maximum (FWHM) of Stark-broadened lines ($\Delta\lambda_{1/2}$) relates to the electron density (in cm^{-3}) through:

$$\Delta\lambda_{1/2}=2\omega(n_e/10^{16})$$

where ω is the Stark broadening parameter (or the electron impact half-width). To enhance the collection efficiency of emission light, the narrowband filter was removed to acquire spectra for the electron density calculation. To provide higher temporal resolution, the gate width was fixed at 100 ns and the gate delay was increased in a step size of 100 ns. Due to the lack of information about the Stark broadening parameter of the Sn I transition ($5s^25p^2$-$5s^25p6s$) at 380.10 nm, the Pb I ($6s^26p^2$-$6s^26p7s$) at 368.35 nm and Cu I (3d94s2- 3d104p) transitions at 510.55 nm were chosen to determine electron density in the Sn-Pb and Cu mixed plasmas, respectively. Lorentz curve fitting was used to evaluate the FWHM of the Pb and Cu lines. The ω parameters of the selected Pb and Cu lines are 1.43 Å and 0.43 Å, respectively. The uncertainties are within 23% and 50%, respectively [24, 25].

Figure 6a shows lateral profiles of the electron density obtained at a 100 ns time delay. As can be seen, a relatively high electron density existed in the center line-of-sight region of the plasma. Similar

distributions of electron density were obtained for later delay times. In all cases, the interpenetration region between the two mixed plasmas maintained a relatively high electron density. The temporal dependence of electron density in the plasma center (line-of-sight) is shown in **Figure 6b**. The average electron density at the plasma center (Y=0 μm) decayed from 1.9×10^{16} cm^{-3} to 4.8×10^{15} cm^{-3} in the time range from 100 ns to 500 ns. The temporal decrease in the electron density follows $n_e \propto t^{-0.87}$, which is similar to the attenuation of densities previously reported in fs laser ablation of Cu [17].

The plasma temperature was calculated using the Boltzmann plot method, assuming that the plasma is in Local Thermodynamic Equilibrium (LTE). The excitation temperature (T_{exc}) can be determined by [26]:

$$\ln[(\lambda_{ij}I_{ij})/(g_iA_{ij})] = -E_i/KT+\ln[(N(T_{exc})/U(T_{exc})]$$

where I_{ij}, λ_{ij}, A_{ij}, g_i, and E_i are the intensity, wavelength, transition probability, statistical weight, and energy of the upper state i, K is Boltzmann constant, $U(T_{exc})$ is the partition function and $N(T_{exc})$ is the total number density. The temperatures of Cu and Sn-Pb mixed plasmas were derived from the Cu I lines (510.55 nm, 515.32 nm and 521.82 nm) and Pb I lines (368.35 nm and 373.99 nm). The lateral (horizontal) profile of the temperature obtained at a delay time of 100 ns is shown in **Figure 6a**. The temperature exhibited an obvious drop at the outer edges of the plasma, where the electron density was also relatively low. During plasma expansion, atoms were compressed against the surrounding gas, and the outer plasma emission species were cooled by collisions with the ambient air. The evolution of the measured plasma excitation temperature as a function of delay time is shown in **Figure 6b**. The average plasma excitation temperatures at the interface (Y=0 μm) and Cu mixed plasma center (Y=-66 μm) were found to decrease with a similar decay, proportional to $t^{-0.22}$ and $t^{-0.25}$ from approximately 12000 K to 8000 K, as the delay time increased from 100 to 700 ns, meanwhile the Cu plasma mixing degree increased from about 19% to 37%. These results show that the plasma core from the Cu plasma center to the Sn-Pb plasma center maintained a relatively high temperature and electron density during the mixing between the two plasmas.

Conclusion

We studied the interfacial mixing dynamics of two isolated laser-induced plasmas formed at the boundary between two metals (Cu and Sn-Pb) using femtosecond laser ablation. Unlike the outer horizontal and vertical plasma expansion velocity which changes with time, mixing processes occurred with a fairly constant speed (v_M) of ~10^4 cm/s. Interfacial plasma mixing processes are very important at early times in these fs-plasmas, and continue taking place until the very end of the plasma persistence. The two model metals used in this initial study were purposely chosen to have nominal surface roughness so as to evaluate solely the plasma mixing processes, without accounting for morphological variations over the sample which are likely to further affect the plasma mixing processes and chemistry. This work provides insights into the importance of interfacial mixing processes, which should be carefully evaluated as potentially highly influential factors in sampling across inhomogeneous media in chemical analysis and chemical imaging applications.

Acknowledgements

This research was supported by the US Department of Energy, Office of Defense Nuclear Nonproliferation Research and Development, under contract number DE-AC02-05CH11231 at the Lawrence Berkeley National Laboratory. This work was also supported by the National Science Foundation of China (No. 11705020), Liaoning Provincial Natural Science Foundation of China (No. 20170540153) and National Key R&D Program of China (No. 2017YFA0402500). Ran Hai acknowledges support from the China Scholarship Council (CSC).

Figure Captions:

Figure 1: Schematic of the experimental system

Figure 2: Time-resolved images of fs laser ablation obtained using an ICCD camera: (a) temporal evolution of Cu/Sn-Pb plasma emission through a 514.5 nm filter to extract the emission of Cu, (b) temporal evolution of Cu/Sn-Pb plasma emission through a 380 nm filter to extract the emission of Sn, (c) temporal evolution of pure Cu plasma using a 514.5 nm filter, and (d) temporal evolution of Sn-Pb plasma using a 380 nm filter. All the images were normalized to their maximum intensity. The white dashed line corresponds to the position of the Cu/Sn-Pb interface.

Figure 3: Emission spectra from the Cu/Sn-Pb sample interface at different distances from the Cu/Sn-Pb interface (along Y axis), at a time delay of 100 ns with a gate width of 100 ns. (a) Spectra obtained using a Cu narrowband filter. (b) Spectra obtained using a Sn narrowband filter. (c) The ratio of atomic line intensity over the total emission intensity for Cu and Sn as a function of horizontal distance. (d) Depth profile of a Cu/Sn-Pb crater obtained after ablation with 5 pulses with the beam centered at the interface between the two materials.

Figure 4: Spatial distribution of Cu (black color) and Sn (red color) emission intensity from the Cu/Sn-Pb plasma at different delay times. All images were normalized to the maximum intensity of each plasma. The Sn-Pb plasma schematic diagram on the right is drawn larger than the Cu-plasma for clarity of axis labelling.

Figure 5: (a) Position-time (*R*-*t*) plots of horizontal and vertical expansion of pure Cu and pure Sn plasma. (b) Position-time (*R*-*t*) plots of internal mixing in Cu-Sn plasma. (c) Temporal variation of velocities of horizontal outside expansion and internal mixing. (d) Temporal variation of the mixing degree *r*. The symbols represent experimental data points and curves represents fitting lines.

Figure 6: (a) Typical lateral profiles of the excitation temperature (left axis) and electron density (right axis) at gate delay of 100 ns. (b) Time resolved excitation temperature (left axis) and electron density (right axis) at different lateral y positions. Time zero corresponded to the firing of the femtosecond laser

pulse. The electron density was determined spectroscopically through the Stark-broadened linewidths of the Pb I 368.35 nm. The plasma temperature was determined from the intensity ratios of the Cu I 510.55 nm line and Cu I 521.82 nm line.

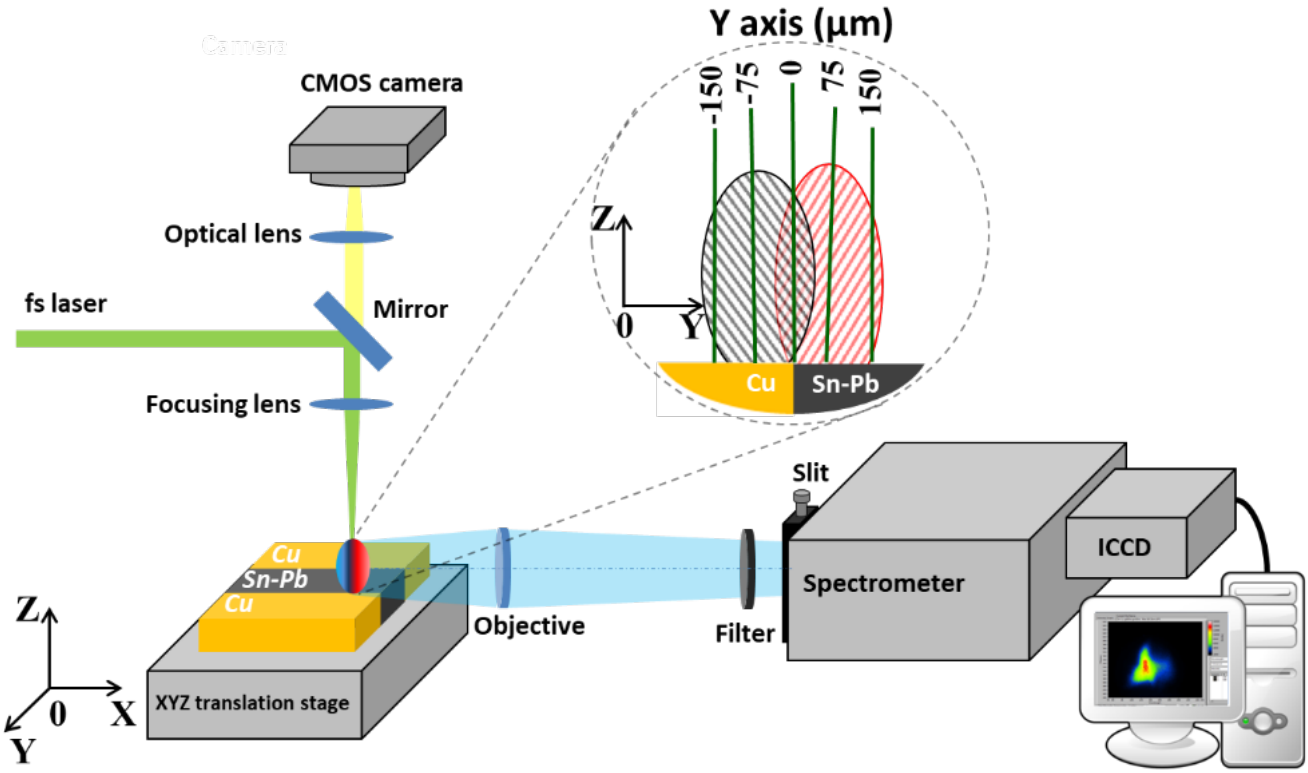

Figure 1 Schematic of the experimental system

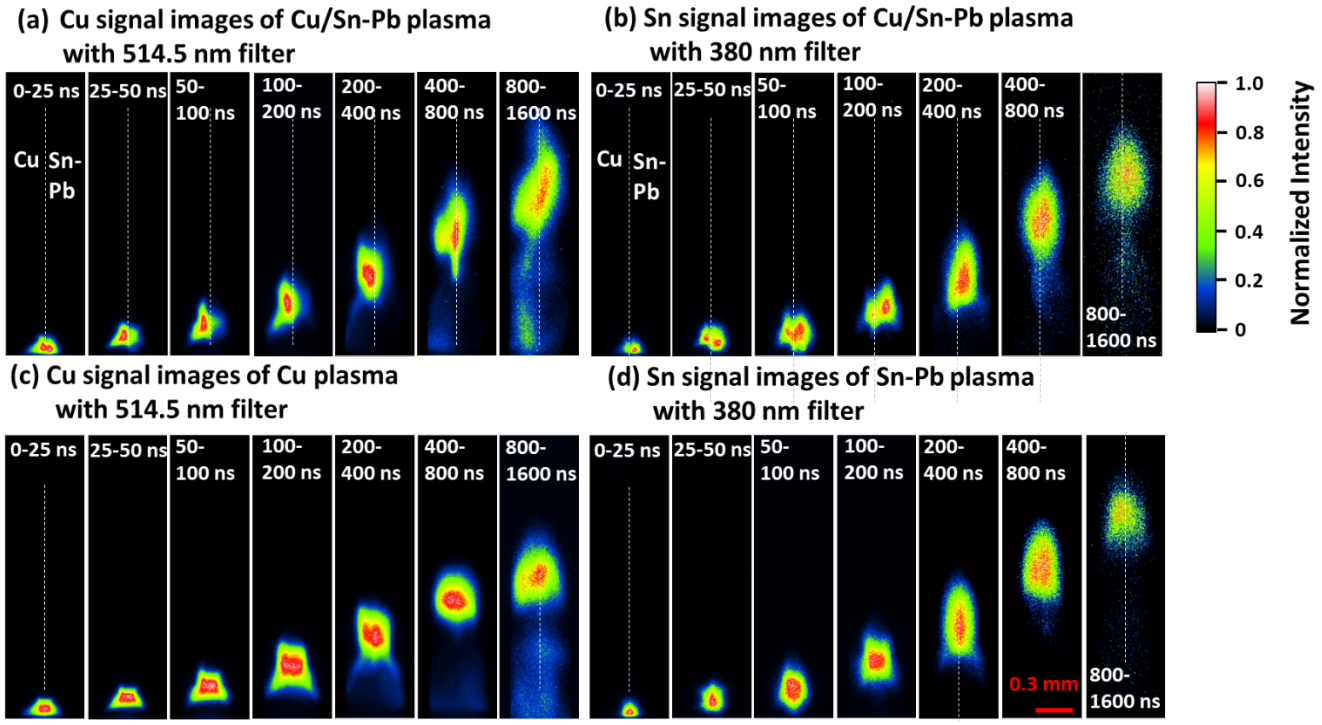

Figure 2. Time-resolved images of fs laser ablation obtained using an ICCD camera: (a) temporal evolution of Cu/Sn-Pb plasma emission through a 514.5 nm filter to extract the emission of Cu, (b) temporal evolution of Cu/Sn-Pb plasma emission through a 380 nm filter to extract the emission of Sn, (c) temporal evolution of pure Cu plasma using a 514.5 nm filter, and (d) temporal evolution of Sn-Pb plasma using a 380 nm filter. All the images were normalized to their maximum intensity. The white dashed line corresponds to the position of the Cu/Sn-Pb interface.

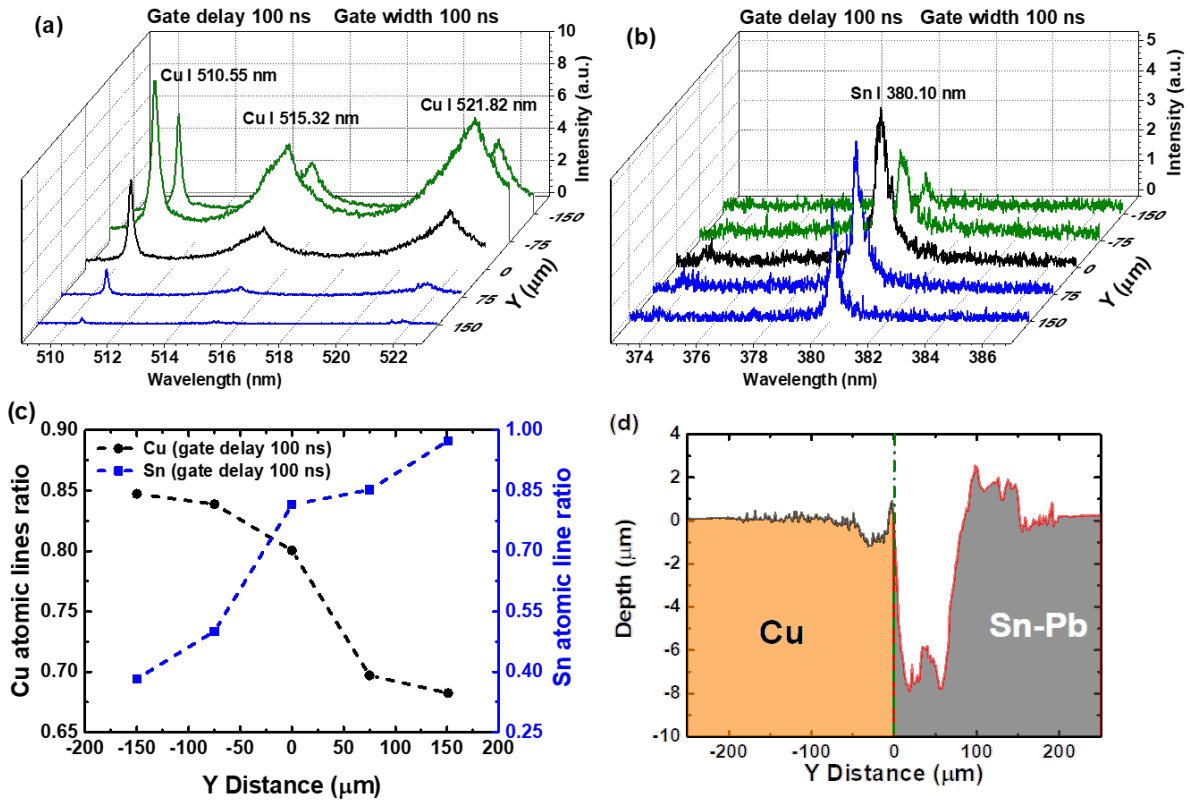

Figure 3. Emission spectra from the Cu/Sn-Pb sample interface at different distances from the Cu/Sn-Pb interface (along Y axis), at a time delay of 100 ns with a gate width of 100 ns. (a) Spectra obtained using a Cu narrowband filter. (b) Spectra obtained using a Sn narrowband filter. (c) The ratio of atomic line intensity over the total emission intensity for Cu and Sn as a function of horizontal distance. (d) Depth profile of a Cu/Sn-Pb crater obtained after ablation with 5 pulses with the beam centered at the interface between the two materials.

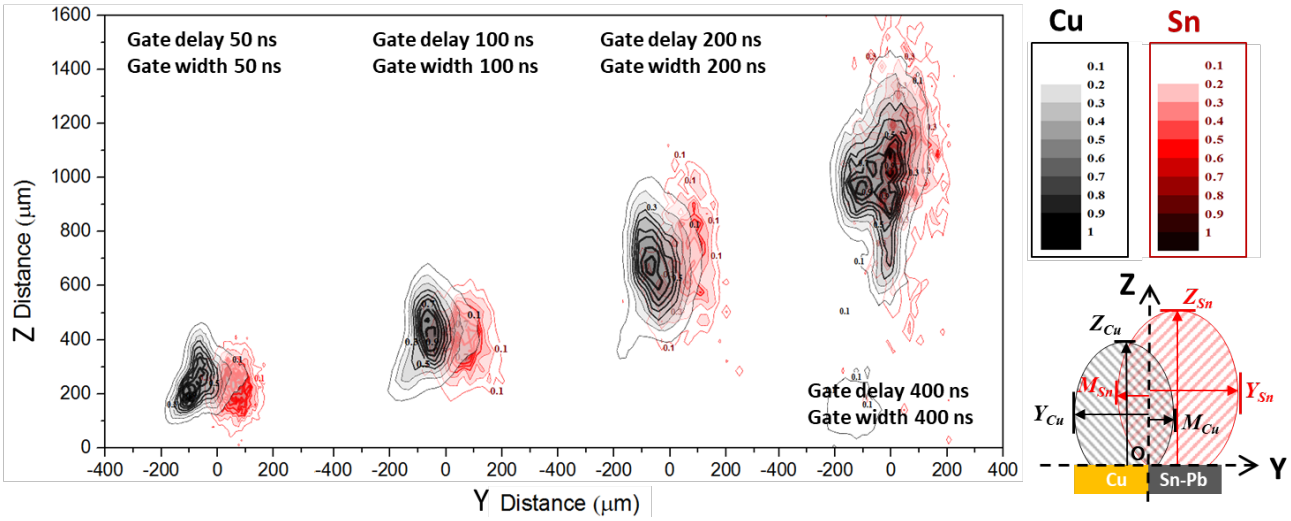

Figure 4. Spatial distribution of Cu (black color) and Sn (red color) emission intensity from the Cu/Sn-Pb plasma at different delay times. All images were normalized to the maximum intensity of each plasma. The Sn-Pb plasma schematic diagram on the right is drawn larger than the Cu-plasma for clarity of axis labelling.

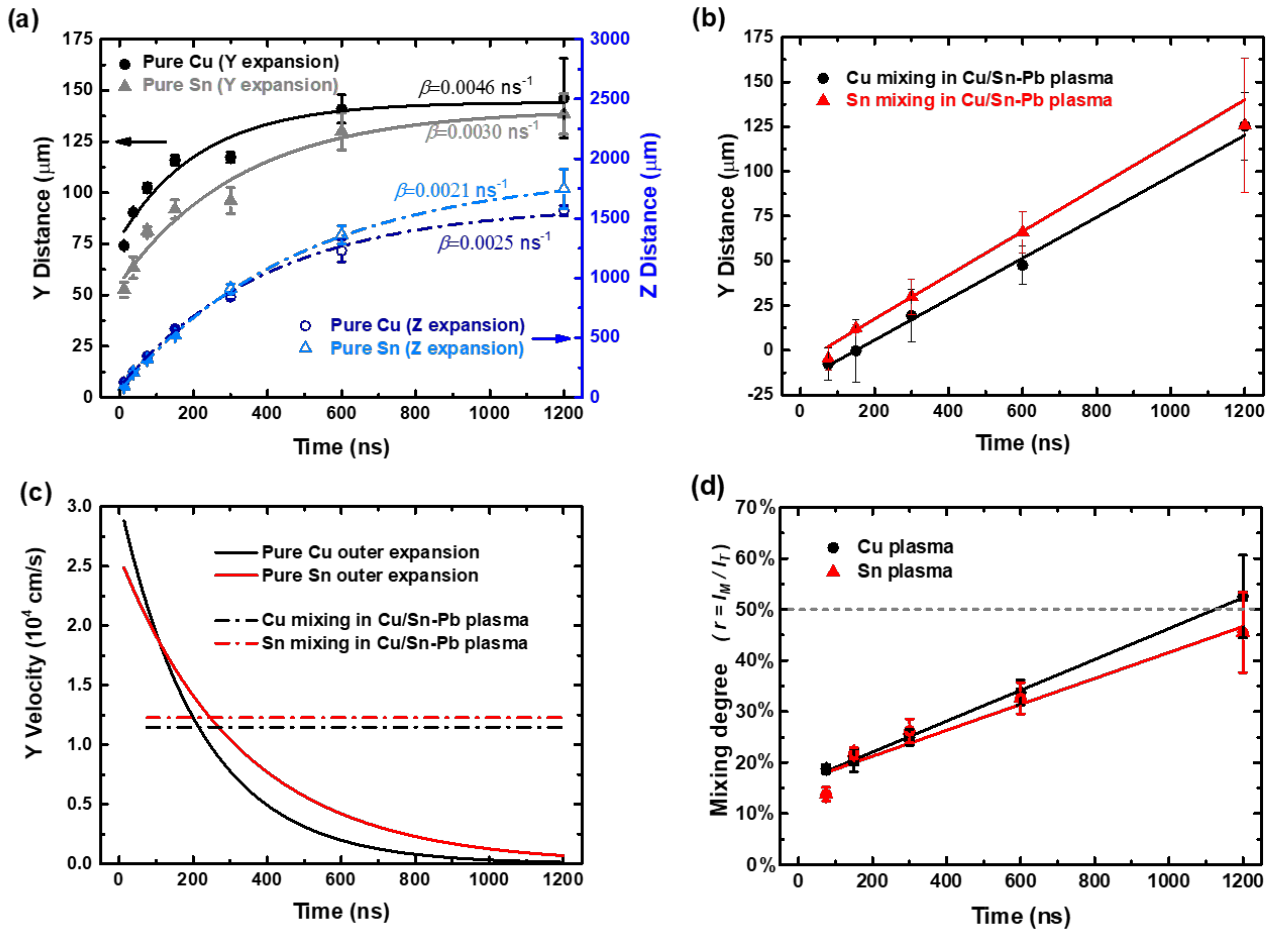

Figure 5 (a) Position-time (*R-t*) plots of horizontal and vertical expansion of pure Cu and pure Sn plasma. (b) Position-time (*R-t*) plots of internal mixing in Cu-Sn plasma. (c) Temporal variation of velocities of horizontal outside expansion and internal mixing. (d) Temporal variation of the mixing degree *r*. The symbols represent experimental data points and curves represents fitting lines.

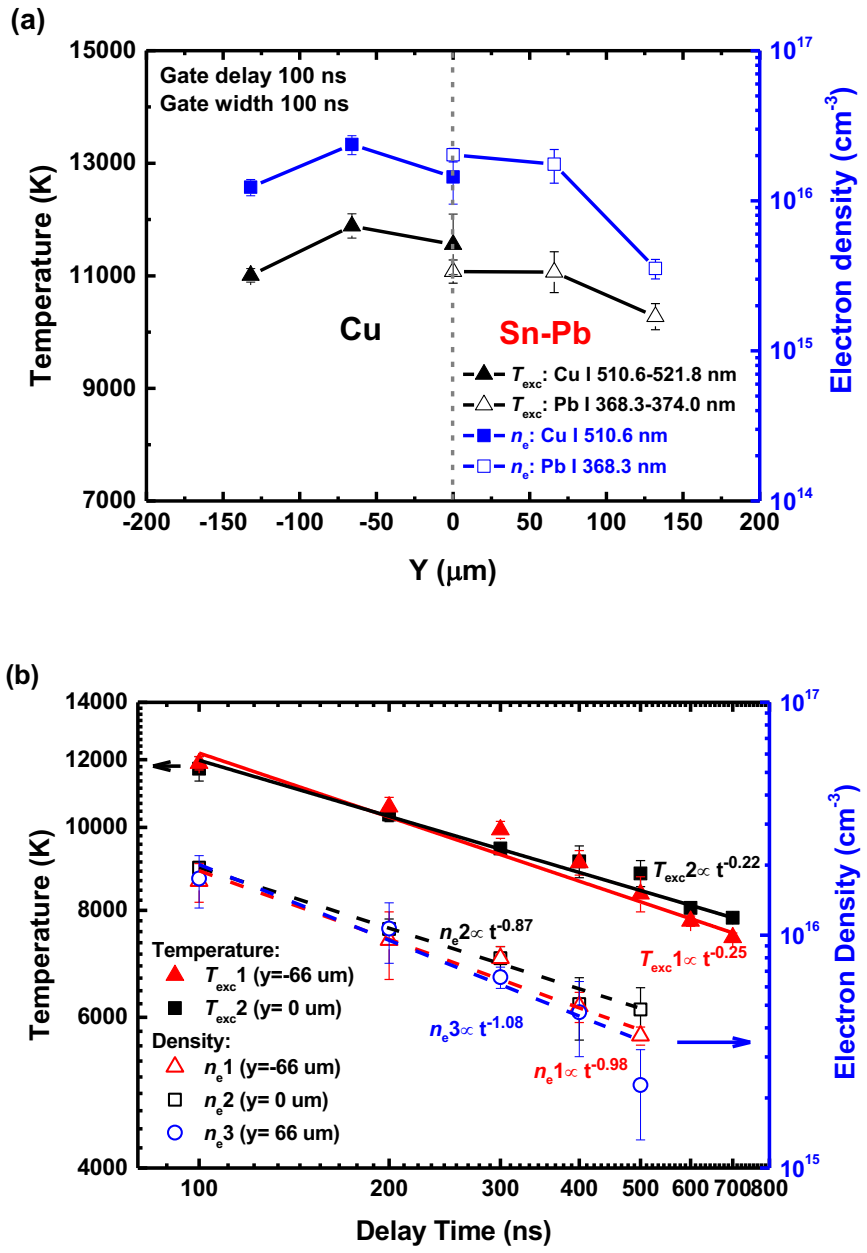

Figure 6. (a) Typical lateral profiles of the excitation temperature (left axis) and electron density (right axis) at gate delay of 100 ns. (b) Time resolved excitation temperature (left axis) and electron density (right axis) at different lateral y positions. Time zero corresponded to the firing of the femtosecond laser pulse. The electron density was determined spectroscopically through the Stark-broadened linewidths of the Pb I 368.35 nm. The plasma temperature was determined from the intensity ratios of the Cu I 510.55 nm line and Cu I 521.82 nm line.

References

1. D. A. Cremers, L.J. Radziemski, Handbook of Laser-Induced Breakdown Spectroscopy, John Wiley & Sons, Ltd., Chichester, 2006.
2. L. Moenke-Blankeburg, T. Schumann, J. Nölte, Direct solid soil analysis by laser-ablation inductively-coupled plasma-atomic emission-spectrometry, J.Anal. At. Spectrom. 9 (1994) 1059-1062.
3. R. E. Russo, X. L. Mao, H. C. Liu, J. Gonzalez, S. S. Mao, Laser ablation in analytical chemistry-a review, Talanta 57 (2002) 425-451.
4. H. Kim, A. Piqué, J. S. Horwitz, H. Murata, Z. H. Kafafi, C. M. Gilmore, D. B. Chrisey, Effect of aluminum doping on zinc oxide thin films grown by pulsed laser deposition for organic light-emitting devices, Thin Solid Films 377 (2000) 798-802.
5. A. M. Morales, C. M. Lieber, A laser ablation method for the synthesis of crystalline semiconductor nanowires, Science 279 (1998) 208.
6. R. R. Gattass, E. Mazur, Femtosecond laser micromachining in transparent materials, Nat. Photonics 2 (2008) 219-225.
7. J. Lettry, R. Catherall, G. J. Focker, O. C. Jonsson, E. Kugler, H. Ravn, C. Tamburella, V. Fedoseyev, V. I. Mishin, G. Huber, V. Sebastian, M. Koizumi, U. Koster and the ISOLDE Collaboration, Recent developments of the ISOLDE laser ion source, Rev. Sci. Instrum. 69 (1998) 761-763.
8. D. W. Hahn, N. Omenetto, Laser-induced breakdown spectroscopy (LIBS), part II: review of instrumental and methodological approaches to material analysis and applications to different fields, Appl. Spectrosc. 66 (2012) 347–419.
9. R. E. Russo, T.W. Suen, A.A. Bol'shakov, J. Yoo, O. Sorkhabi, X.L. Mao, J.J. Gonzalez, D. Oropeza, V. Zorba, Laser Plasma Spectrochemistry, J. Anal. At. Spectrom. 26 (2011) 1596.
10. R. Hai, N. Farid, D. Zhao, L. Zhang, J. Liu, H. Ding, J.Wu, G.N. Luo, Laser-induced breakdown spectroscopic characterization of impurity deposition on the first wall of a magnetically confined fusion device: Experimental Advanced Superconducting Tokamak, Spectrochim. Acta Part B 87 (2013) 147–152.
11. V. Motto-Ros, L. Sancey, X.C.Wang, Q.L. Ma, F. Lux, X.S. Bai, G. Panczer, O. Tillement, J. Yu, Mapping nanoparticles injected into a biological tissue using laser-induced breakdown spectroscopy, Spectrochim. Acta Part B 87 (2013) 168-174.
12. H. Hou, L. Cheng, T. Richardson, G. Chen, M. Doeff, R. Zheng, R. Russo, V. Zorba, Three-dimensional elemental imaging of Li-ion solid-state electrolytes using fs-laser induced breakdown spectroscopy (LIBS), J. Anal. At. Spectrom. 30 (2015) 2295-2302.
13. F. Trichard, L. Sorbier, S. Moncayo, Y. Blouet, C.P. Lienemann, V. Motto-Ros, Quantitative elemental imaging of heterogeneous catalysts using laser-induced breakdown spectroscopy, Spectrochim. Acta B 133 (2017) 45-51.
14. B.N. Chichkov, C. Momma, S. Nolte, F. von Alvensleben, A. Tünnermann, Femtosecond, picosecond and nanosecond laser ablation of solids, Appl. Phys. A Mater. Sci.Process. 63 (1996) 109-115.

15. V. Margetic, A. Pakulev, A. Stockhaus, M. Bolshov, K. Niemax, R. Hergenröder, A comparison of nanosecond and femtosecond laser-induced plasma spectroscopy of brass samples, Spectrochim. Acta Part B 55(2000), 1771-1785.
16. V. Zorba, J. Sysdek, X. Mao, R. E. Russo, R. Kostecki, Ultrafast laser induced breakdown spectroscopy of electrode/electrolyte interfaces, Appl. Phys. Lett. 100 (2012) 234101.
17. V. Zorba, X. Mao, R.E. Russo, Femtosecond laser induced breakdown spectroscopy of Cu at the micron/sub-micron scale, Spectrochim. Acta Part B 113 (2015) 37-42.
18. X. H. Zeng, S. S. Mao, C. Y. Liu, X. L. Mao, R. Greif, R. E. Russo, Plasma diagnostics during laser ablation in a cavity, Spectrochim. Acta Part B 58 (2003) 867-877.
19. A. Elhassan, A. Giakoumaki, D. Anglos, G. M. Ingo, L. Robbiola, M. A. Harith, Nanosecond and femtosecond laser induced breakdown spectroscopic analysis of bronze alloys, Spectrochim. Acta Part B 63 (2008) 504-511.
20. S.S. Harilal, C.V. Bindhu, M.S. Tillack, F. Najmabadi, A.C. Gaeris, Internal structure and expansion dynamics of laser ablation plumes into ambient gases, J. Appl. Phys. 93 (2003) 2380-2388.
21. D.B. Geohegan, Physics and diagnostics of laser plume propagation for high-Tc superconductor film growth, Thin Solid Films 220 (1992) 138-145.
22. N. Farid, S. S. Harilal, H. Ding, A. Hassanein, Dynamics of ultrafast laser plasma expansion in the presence of an ambient, Appl. Phys. Lett. 103, (2013) 191112
23. J. P. Singh, S. N. Thakur, Laser-Induced Breadown Spectroscopy, First, Elsevier, 2007.
24. N. Konjević, A. Lesage, J.R. Fuhr, W. L. Wiese, Experimental Stark widths and shifts for spectral lines of neutral and ionized atoms (a critical review of selected data for the period 1989 through 2000), J. Phys. Chem. Ref. Data 31 (2002) 819-927
25. N. Konjević, W. L. Wiese, Experimental Stark widths and shifts for spectral lines of neutral and ionized atoms, J. Phys. Chem. Ref. Data 19 (1990) 1307-1385.
26. C. Aragón, J. A. Aguilera, Characterization of laser induced plasmas by optical emission spectroscopy: A review of experiments and methods, Spectrochim. Acta Part B 63 (2008) 893-916.